Nano Research Energy

ISSN 2791-0091 (print); 2790-8119 (online)
https://doi.org/10.26599/NRE.2024.9120129

Research Article

FeCoP sub-nanometric-sheets for electrocatalzing overall water splitting

Long Zhao[1], Kexin Meng[1], Yibo Guo[2], Qingsheng Wu[1], Quanjing Zhu[1], Tao Zhou[1], Yongqing Fu[3], and Ming Wen[1] (✉)

[1] School of Chemical Science and Engineering, School of Environmental Science and Engineering, Shanghai Key Laboratory of Chemical Assessment and Sustainability, State Key Laboratory of Pollution Control and Resource Reuse, Tongji University, Shanghai 200092, China
[2] College of Bioengineering, East China University of Science and Technology, Shanghai 200237, China
[3] Faculty of Engineering and Environment, Northumbria University, Newcastle upon Tyne NE99, UK

Received: 21 April 2024 / **Revised:** 2 June 2024 / **Accepted:** 20 June 2024

ABSTRACT

Renewable electrical energy for electrolysis water can achieve green industrial chains for hydrogen production. However, finding efficient electrocatalysts remains a challenge for green hydrogen. Herein, sub-nanometric FeCoP nanosheets with average thickness of 0.9 nm is constructed through 2D self-assembly driven by cavitation effect of ultrasonics and following phosphating. Benefiting from abundant active sites, enhanced H_2O molecular adsorption kinetics, and highly enhanced structural stability, the subcrystalline FeCoP shows excellent electrocatalytic activities of hydrogen evolution reaction (HER) and oxygen evolution reactions (OER). Ultralow overpotential of 37 mV is achieved at 10 $mA \cdot cm^{-2}$ for HER. When the FeCoP catalyst was used as both cathode and anode for overall water splitting using renewable electrical energy, green hydrogen produced is directly applied for hydrogen fuel cell to drive fan for more than 10 h. Theoretical calculation indicates that subcrystalline FeCoP more easily adsorbs H_2O than crystalline one and thus speeds up the kinetics of Volmer step in HER process.

KEYWORDS

green hydrogen energy, subcrystalline, overall water splitting, sub-nanometric-sheets

1 Introduction

Green hydrogen energy, as one of efficient and clean energy sources, refers to the production of hydrogen through water electrolysis using renewable energy sources [1, 2]. Current water electrolysis technology consumes significant amounts of electrical energy generated from the conventionally power generation methods, conflicting with the global objectives of energy structure transition and emission reduction. Solar energy, as a renewable and non-polluting source, can be directly converted into electrical energy using photovoltaic system and then supplied to achieve water electrolysis to obtain green hydrogen. This process allows the entire industrial chain of hydrogen production and also the end users to give up fossil fuels, and make great effort to achieve zero-emission and sustainable energy development [3, 4]. The key challenges for current green hydrogen generation technologies are the economical and efficient electrocatalysts [5]. Recently, transition metal phosphides (TMPs) act as bifunctional electrocatalysts for cathodic hydrogen evolution reaction (HER) and anodic oxygen evolution reactions (OER), which has demonstrated impressive efficiency as the replacement for noble metals [6–9]. Moreover, it is reported that the surface of crystalline TMPs electrocatalysts will be *in-situ* transformed into subcrystalline structure or even completely amorphous structures during the electrochemical water splitting, which can be served as active species for electrochemical reactions [10–13]. Compared with the crystalline materials, these subcrystalline catalysts have uniquely chemical homogeneity, atomic-scale structural flexibility, and abundant defects [14]. Numerous defects and dangling bonds effectively enhance their intrinsic activity and electrochemical stability [15, 16]. The structural flexibility facilitates *in-situ* transformation from originally inert species into active species during the catalytical process [17, 18]. Due to these positive factors, these subcrystalline structures effectively circumvent the sluggish kinetics of HER and/or OER which are commonly occurring in those crystalline catalysts, thereby being able to achieve superior performance for electrochemical water splitting. However, after those crystalline structures are *in-situ* transformed into subcrystalline or even amorphous layers, their conductivity is decreased. Thus, understanding the electrocatalytic water splitting mechanism of directly synthesized subcrystalline TMPs nanomaterials is crucial and urgent for the design and production of efficient and low-cost electrocatalysts.

Address correspondence to Ming Wen, m_wen@tongji.edu.cn

In this work, subcrystalline FeCoP ultrathin nanosheets have been constructed through 2D self-assembly driven by cavitation-effect induced by ultrasonics followed by the post-phosphating process. The following three advantages enable the obtained FeCoP catalyst to achieve superior electrocatalytic performance for water splitting. Firstly, the abundant active sites have been achieved from sub-nanometric thickness and formation of unsaturated atomic defects in subcrystalline structure, which is beneficial to reduce the activation energy, thereby increasing the reaction rate. Secondly, the adsorption energy can be optimized by reconstructing the d-electronic configuration of Co, which provides a suitable kinetic behavior of H_2O in electrocatalytic reaction. Thirdly, a high structure stability can be maintained by forming these subcrystalline structures with a short-range order, which can effectively extend the service life of the catalyst. Meanwhile, our theoretical calculation reveals that the subcrystalline FeCoP is more liable to adsorb H_2O molecules than the crystalline ones, thus speeding up the kinetics of Volmer step. Thus, as-synthesized subcrystalline FeCoP ultrathin nanosheets have the ultralow overpotentials of 37 and 290 mV at the current densities of 10 mA·cm^{-2} for HER and OER, respectively. When employed as both the anode and cathode for overall water splitting, the FeCoP can achieve current densities of 10 and 196 mA·cm^{-2} at the low potentials of 1.50 and 1.80 V vs. RHE. Utilizing photovoltaic systems for the conversion of solar energy into electrical power to water electrolysis, the generated green hydrogen can be seamlessly applied into the hydrogen fuel cell to sustain operational continuity of fan for over 10 h. This work provides a strategy of achieving zero emissions and sustainable development for applying subcrystalline and ultrathin nanoalloys as efficient and durable electrocatalysts toward water splitting and hydrogen energy production.

2 Experimental

2.1 Materials and reagents

Cobalt chloride ($CoCl_2·6H_2O$, 98%), ferric chloride ($FeCl_3·6H_2O$, 98%), sodium borohydride ($NaBH_4$, 98%), sodium hypophosphite monohydrate ($NaH_2PO_2·H_2O$, 99%), 20% PtC, and RuO_2 were purchased from Aladdin Biochemical Technology Co., Ltd., Shanghai, China.

2.2 Synthesis of subcrystalline FeCoP

Typically, FeCoP sub-nanometric-sheets was prepared using $FeCo(OH)_2$ as the precursor and NaH_2PO_2 as the phosphorus source. Firstly, 40 mL of 0.07 mmol·L^{-1} $CoCl_2·6H_2O$ and 0.007 mol·L^{-1} $FeCl_3·6H_2O$ solution were mixed and placed in an ultrasonic reactor. Then, with the agitation of ultrasound, the freshly prepared $NaBH_4$ solution (20 mg $NaBH_4$ dissolved in 40 mL water) at an ice condition was added dropwise. After 120 min of reaction, the $FeCo(OH)_2$ precursor was collected by centrifugation and washed with ethanol and water for several times. Subsequently, 1.00 g of NaH_2PO_2 was placed on the upwind side of a tubular furnace while $FeCo(OH)_2$ precursor (10 mg) was placed on the downwind side. Subcrystalline FeCoP ultrathin nanosheets was finally obtained at the phosphating treatment at 300 °C with a heating rate of 2 °C·min^{-1} for 1 h under an Ar atmosphere.

2.3 Characterization

Morphologies of the samples were investigated using a field emission scanning electron microscope (SEM, HITACHIS-4800, Japan) and a high-resolution transmission electron microscope (HR-TEM, JEM-2100, Japan). Amount and distributions of elements inside the catalysts were obtained using an energy-dispersive X-ray spectroscope (EDS) with elemental mapping functions. Thickness of the as-obtained materials was measured using an atomic force microscope (AFM, Multimode Nanoscope VIII, America). Crystalline phases of FeCoP samples were obtained using an X-ray diffractometer (XRD, D/max-RB, Germany) with Cu-Kα radiation source within 2θ of 10°–70°. An X-ray photoelectron spectroscope (XPS, PHI-5000C ESCA, America) with a monochromatic Mg-Kα radiation as the X-ray source was used to detect the chemical element compositions and their valence states. A Fourier transform infrared spectroscope (FTIR, Nexus 670, America) was utilized to measure the changes of O-H bonding state within a range of 400–4000 cm^{-1} and with a resolution of 1 cm^{-1}.

2.4 Electrochemical measurements

Electrochemical performance of the as-prepared catalysts was evaluated with a three-electrode configuration by using an electrochemical workstation (CHI 760E, Chenhua, Shanghai, China) in a solution of 1 M KOH. The measurements were carried out at room temperature in the 1 M KOH electrolyte with a pH value of 14, after blowing the liquid with O_2 for 30 min for OER and N_2 for HER. Specifically, glassy carbon electrode (GCE) was used as the working electrode, graphite rod (Alfa Aesar, 99.9995%) as the counter electrode, and standard Hg/HgO as the reference electrode. The following equation was used to convert the tested potential into reversible hydrogen electrode potential (RHE):

$$E_{\mathrm{RHE}} = E^{\theta} + 0.059 \times \mathrm{pH} + E_{\mathrm{test}} + \mathrm{IR}_{\mathrm{correct}} \quad (1)$$

To evaluate the electrochemical properties of FeCoP, electrode slurry was prepared by mixing 4 mg catalyst powder, 10 μL Nafion (5%), 250 μL isopropyl alcohol, and 750 μL deionized water. Then 10 μL of such uniformly dispersed slurry after ultrasonic stirring was dropped onto the GCE with an area of 0.07065 cm^2 and then left for natural drying to form the working electrode. Cyclic voltammetry (CV) tests were implemented at a scan rate of 50 mV·s^{-1} for at least 20 cycles to activate the electrocatalysts. Linear sweep voltametry (LSV) tests were performed at a scan rate of 2 mV·s^{-1}. The electric double layer capacitance (C_{dl}) was estimated from the CV tests at different scan rates of 20, 40, 60, 80, and 100 mV·s^{-1}. Measurement of electrochemical impedance spectroscopy (EIS) was carried out to evaluate electron transfer capability of electrocatalysts with potential amplitude of 5 mV, and within a frequency range of 0.01–105 Hz. The electrochemically active surface area (ECSA) values of prepared samples were calculated using Eq. (2)

$$\mathrm{ECSA} = C_{\mathrm{dl}}/C_{\mathrm{s}} \quad (2)$$

C_{s} is the specific capacitance which is generally between 20 to 60 μF·cm^{-2} in an alkaline media. In this study, we chose the midpoint-specific capacitance of 40 μF·cm^{-2}. The turnover frequency (TOF) which is defined as the number of oxygen molecules produced per second per active site was calculated using Eq. (3)

$$n = Q/2F \quad (3)$$

where n is the number of active sites, F is the Faraday constant, and Q is the whole charge of CV curve, respectively.

Assuming that all of active sites were entirely accessible to the electrolyte, the TOF values were calculated. The Eq. (4) was used to calculate TOF:

$$\mathrm{TOF} = j/2nF \quad (4)$$

where F and n are the Faraday constant and the number of active sites, respectively; j is the current density of LSV curves.

Faradaic efficiency (FE) for both the HER and OER was determined by monitoring O_2 evolution, and the amount of evolved H_2 and O_2 during electrolysis was quantified using the gas chromatography (GC, with a carrier gas of N_2; chromatographic column of 5 Å, molecular sieve column, and thermal conductivity detector). The theoretical oxygen production was determined by dividing the charge by $4F$ (F = Faraday constant):

$$\mathrm{FE} = (n_{\mathrm{meas.gas}}/n_{\mathrm{calcd.gas}}) \times 100\% \quad (5)$$

Before each measurement, the electrolyte was bubbled with N_2 gas for 30 min. The amount of H_2 and O_2 produced was quantified by injecting 0.6 μL gas pumped from the electrolytic cell through a micro-sampler into the GC.

2.5 Theoretical calculation procedures

Theoretical calculation of adsorption energy of H_2O molecules for both low and high crystalline phases was performed using a cluster model method, and the adsorption energy of crystal structures was calculated using isolated systems. During structural optimization processes, all the edge's unsaturated atoms except for the adsorption area were frozen. The structural optimization calculation level was PBE0-D3 (BJ)/def2-SV (P), and the addition of the SlowConv keyword made the system SCF more easily converged. The calculation level of single point energy was set as PBE0-D3 (BJ)/def2-TZVP. The calculation of adsorption energy was the single point energy of the complex minus the single point energy of two monomers.

3 Results and discussion

3.1 Design and fabrication

Figure 1 shows the fabrication process and structural characterization of the subcrystalline FeCoP ultrathin nanosheets. It has been constructed through a 2D self-assembly process driven by cavitation-effect of ultrasonics with the followed phosphating process. Initially, cavitation bubbles are formed mainly due to the high-frequency oscillation in the liquid induced by ultrasound. When these cavitation bubbles are randomly ruptured, the locally generated high-speed micro-jets and shock waves effectively cause high-speed collision of Fe^{3+}/Co^{2+} ions, which are then reacted with OH^- (derived from BH_4^+) to form $FeCo(OH)_2$ by adjusting the doping ratio of Fe (Fig. S1 in the Electronic Supplementary Materials (ESM)). The cavitation effect of ultrasound not only slows down the rapid growth of initial crystal nuclei, but also prevents their further aggregation. The self-assembly finally becomes 2D ultrathin nanosheets structures. As the decomposition of NaH_2PO_2 into PH_3 reacts with $FeCo(OH)_2$ during the subsequent phosphating process, thus the subcrystalline FeCoP ultrathin nanosheets is obtained by controlling the phosphating conditions (Figs. S2–S4 in the ESM).

Figure 1 shows the fabrication process and structural characterization of the subcrystalline FeCoP ultrathin nanosheets. It has been constructed through a 2D self-assembly process driven by cavitation-effect of ultrasonics with the followed phosphating process. Initially, cavitation bubbles are formed mainly due to the high-frequency oscillation in the liquid induced by ultrasound. When these cavitation bubbles are randomly ruptured, the locally generated high-speed micro-jets and shock waves effectively cause high-speed collision of Fe^{3+}/Co^{2+} ions, which are then reacted with OH^- (derived from BH_4^+) to form $FeCo(OH)_2$ by adjusting the doping ratio of Fe (Fig. S1 in the ESM). The cavitation effect of ultrasound not only slows down the rapid growth of initial crystal nuclei, but also prevents their further aggregation. The self-assembly finally becomes 2D ultrathin nanosheets structures. As the decomposition of NaH_2PO_2 into PH_3 reacts with $FeCo(OH)_2$ during the subsequent phosphating process, thus the subcrystalline FeCoP ultrathin nanosheets is obtained by controlling the phosphating conditions (Figs. S2–S4 in the ESM).

3.2 Morphologies and structures

SEM and TEM images of FeCoP exhibit well-defined morphologies of ultrathin nanosheets (Figs. 2(a) and 2(b)). Its average thickness is ~0.9 nm, evaluated by AFM analysis (Fig. 2(c)). The subcrystalline feature with a short-range ordered structure of FeCoP is proved by the weak ring-like characteristics of the selected area electron diffraction (SAED) pattern and lack of lattice stripes seen in the HR-TEM image (Fig. 2(d)) [19]. This structure can be further confirmed by XRD analysis results of a typical broad diffraction peak around two theta (2θ) values of 37° (Fig. 2(e) above) [20]. Moreover, compositions of FeCoP obtained from the EDS analysis (Fig. 2(e) below) and elemental mapping results (Fig. 2(f)) display homogeneous distributions of Fe, Co, and P elements in the obtained FeCoP ultrathin nanosheets.

XPS spectra reveal that the elements of Fe, Co, and P are coexisted on the surface of FeCoP, which is consistent with the elemental mapping results. For the FeCoP, high-resolution XPS spectra of Co 2p (Fig. 2(g)) exhibit a spin-orbit doublet of Co $2p_{3/2}$ and Co $2p_{1/2}$ in the Co-P bonds located at 779.3 and 793.8 eV with two satellite peaks at binding energies of 787.2 and 800.3 eV,

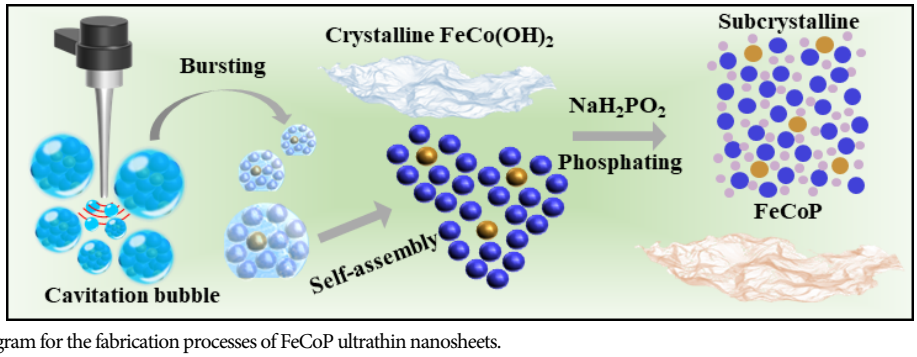

Figure 1 Schematic diagram for the fabrication processes of FeCoP ultrathin nanosheets.

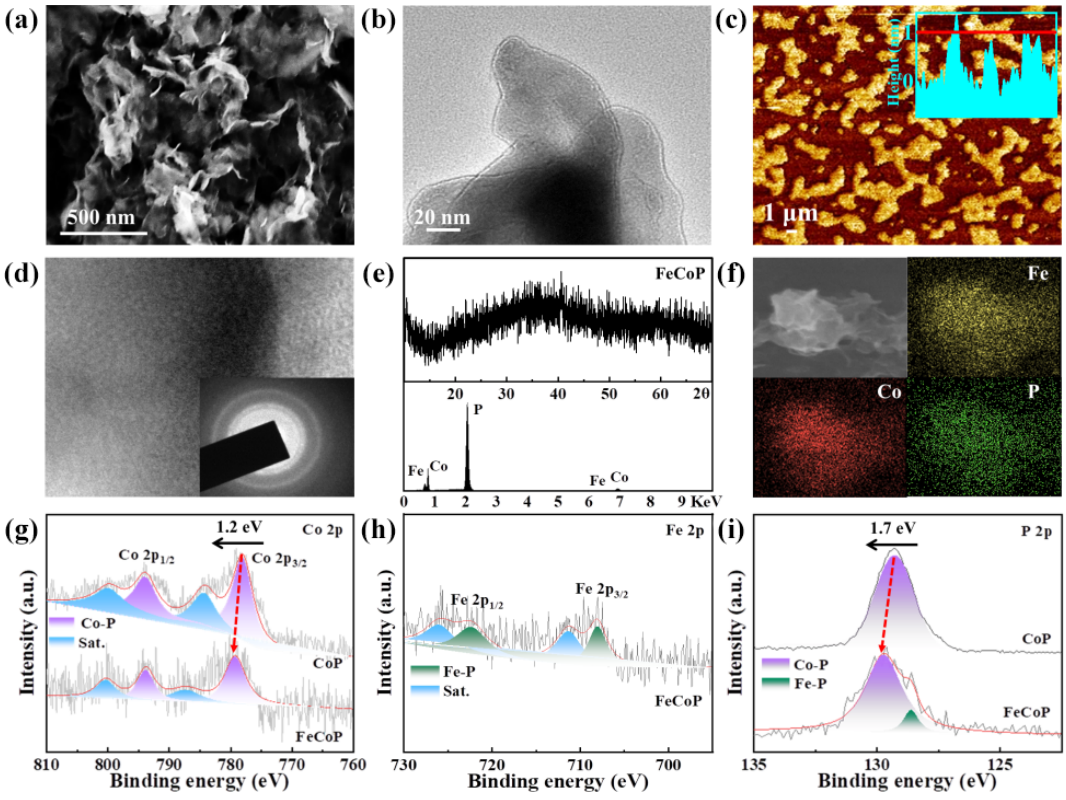

Figure 2 (a) SEM, (b) TEM, (c) AFM, (d) HR-TEM (SAED pattern illustration) images, (e) XRD pattern (above) and EDS spectra (below), (f) elemental mapping, (g)–(i) detail XPS spectra for Co 2p, Fe 2p, and P 2p.

respectively [21, 22]. The binding energies of Co 2p are higher than metallic Co (778.2 eV) [23], indicating that the Co element in the Co-P bonds partially carry positive charges ($Co^{\delta+}$, $0 < \delta < 2$) [24]. It should be noted that the binding energies of Co 2p are shifted to the higher binding energy side compared with those in the CoP sample, demonstrating that there exists electron polarization among Fe, Co, and P elements, which will reduce the energy barrier and increase the catalytic activity [25]. Similarly, the Fe element in the Fe-P also partially carry positive charges ($Fe^{\delta+}$, $0 < \delta < 2$), because the binding energies of Fe 2p spin-orbit doublet (Fig. 2(h), Fe $2p_{3/2}$ and Fe $2p_{1/2}$ at 708.0 and 722.4 eV with two satellite peaks at 711.3 and 726.0 eV) are higher than metallic Fe (707.1 eV) [26]. As for P 2p (Fig. 2(i)), two peaks at 128.6 and 129.7 eV are assigned to the Fe-P and Co-P bonds, respectively [27]. They show negative shifts compared to elemental P (130.2 eV), revealing that the P carries negative charges ($P^{\delta-}$, $\delta < 3$) caused by the occurrence of electron transfer from Fe and Co to P [28]. The binding energy of Co-P bond in FeCoP is shifted to the higher binding energy side if compared with that in CoP sample. This can also prove that the electron configuration is reconstructed after doping with Fe. Because the work function of Co is larger than that of Fe [29], the binding energy of Co-P bond is shifted accordingly.

3.3 Evaluation of electrocatalytic activity

Figure 3 illustrates the electrocatalytic HER performance of the prepared catalysts in a 1.0 M KOH electrolyte. FeCoP only requires a low overpotential of 37 mV to achieve a current density of 10 $mA \cdot cm^{-2}$, which is much lower than those the CoP (228 mV), the benchmark of 20% Pt/C (67 mV), and some reported catalysts (Figs. 3(a) and 3(b) and Fig. S5, and Table S1 in the ESM). The corresponding Tafel slope was calculated to be 71 $mV \cdot dec^{-1}$, which is smaller than the value of the benchmark Pt/C (85 $mV \cdot dec^{-1}$) and close to the theoretical value (~40 $mV \cdot dec^{-1}$) in the alkaline electrolyte (Fig. 3(c)) [30]. This reveals that the HER process on the FeCoP catalysts undergoes a fast Volmer-Heyrovsky pathway [30]. Besides, the collected ECSA is linearly proportional to the value of the C_{dl} derived from the CV curves (Fig. S6 in the ESM), which are 4.8 and 2.4 $mF \cdot cm^{-1}$ for the FeCoP and CoP, respectively, implying that more accessible active sites are accessible for FeCoP (Fig. 3(d)). Moreover, the FeCoP exhibits a larger ECSA value of 120 cm^2 than that of CoP (60 cm^2), and therefore shows a much better electrochemical activity. Moreover, the turnover frequency (TOF) values of the catalysts were calculated to evaluate their intrinsic HER performance. The TOF value of FeCoP is 0.491 s^{-1}. The results of capacitances at different preparation conditions under an HER overpotentials at 10 $mA \cdot cm^{-2}$ were plotted as shown in Fig. S7 in the ESM. The values of C_{dl} exhibit strong correlations with the doping ratio of Fe, phosphorus temperature, time, and dosage, indicating that all the elements of Fe, Co, and P are active sites for HER since the value of C_{dl} is related to the electrochemically active surface sites [31]. Therefore, the high HER activity of FeCoP is mainly originated from the increased numbers of electrochemically active sites and the optimized electron configurations [32].

To evaluate the interfacial charge transfer kinetics, the Nyquist plots were obtained from EIS measurements [33]. The results shown in Fig. 3(e) reveal that the FeCoP possesses the smallest semicircle, corresponding to its smallest charge transfer resistance (R_{ct}). The calculated R_{ct} of FeCoP (26 Ω) is lower than that of CoP (56 Ω), indicating the former's faster electron transfer during the HER process.

To further investigate the nature of charge transfer, the typical *I*-*V* curves of FeCoP is obtained (Fig. S8 in the ESM). The non-linear behavior of these curves clearly proves that the FeCoP retains its metallic property [34]. Durability of FeCoP was

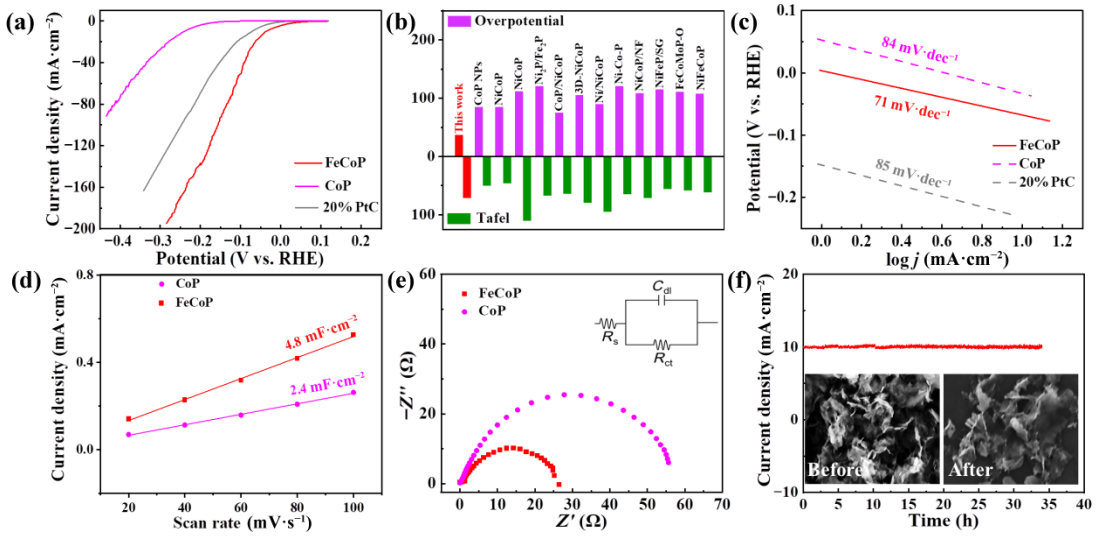

Figure 3 (a) LSV polarization curves, (b) overpotential and Tafel slope comparison with literatures, (c) Tafel slope, (d) dependence of capacitive current on scan rates, (e) Nyquist plots, (f) stability tested using chronoamperometry for HER.

subsequently performed using the chronoamperometric tests for evaluating their practical application potentials, where the current density was maintained at 10 mA·cm^{-2} for 35 h without apparent decay (Fig. 3(f)). In particular, the LSV curves of FeCoP exhibit little changes between the initial results and those after 10,000 cycles (Fig. S9(a) in the ESM), proving the outstanding long-term stability of FeCoP towards HER. The Faraday efficiency of FeCoP for HER was obtained as 96% (Fig. S9(b) in the ESM).

FeCoP was also investigated as OER catalyst and tested in a solution of 1 M KOH (Fig. 4). It shows a low overpotentials of 283 mV at current density of 10 mA·cm^{-2} (Fig. 4(a)), which is comparable to the value of state-of-the-art RuO_2. The current density value obtained is superior to those of RuO_2 and other catalysts (Fig. 4(b) and Fig. S10, Table S2 in the ESM). Figure 4(c) shows the Tafel results of FeCoP and the slope is 48 mV·dec^{-1}, which is much lower than those of CoP (51 mV·dec^{-1}) and benchmarked RuO_2 (54 mV·dec^{-1}). This Tafel slope is ~ 50 mV·dec^{-1}, suggesting that the rate-limiting step is the formation of *OOH (*O + OH$^-$ → *OOH + e$^-$) [35]. According to the classical Butler-Volmer formalism, a smaller Tafel slope indicates that the rate-determining step is closer to the final stages of the multi-electron transfer reaction, which is usually associated to good electrocatalyst.

The C_{dl} value of the FeCoP, obtained by conducting CV tests at a non-faradic potential region (Fig. S11 in the ESM), is 5.3 mF·cm^{-2}. This value is much higher than that of CoP (2.4 mF·cm^{-2}), clearly revealing that the addition of Fe supplies more accessible active sites (Fig. 4(d)) [36]. Moreover, the FeCoP exhibits a larger ECSA value of 132.5 cm^2 than that of CoP (60 cm^2), and therefore shows the former's better electrochemical activity. And the TOF value of FeCoP is 0.313 s^{-1}. EIS analysis manifests that FeCoP has a lower Rct value (270 Ω) compared with that of CoP (295 Ω), which indicates the faster electron transfer in the catalytic HER process (Fig. 4(e)). Figure 4(f) shows that the retention rate is about 99% for the FeCoP at 1.52 V vs. RHE after 20 h chronoamperometric test, which shows an excellent cycling stability. As depicted in Fig. S12(a) in the ESM, the polarization curve obtained after 10,000 continuous CV cycles only shows a deactivation ratio of 6%. Meanwhile, the FeCoP produces a Faraday efficiency of up to 97% for OER (Fig. S12(b) in the ESM).

To further verify the accelerated water splitting effect, FTIR was

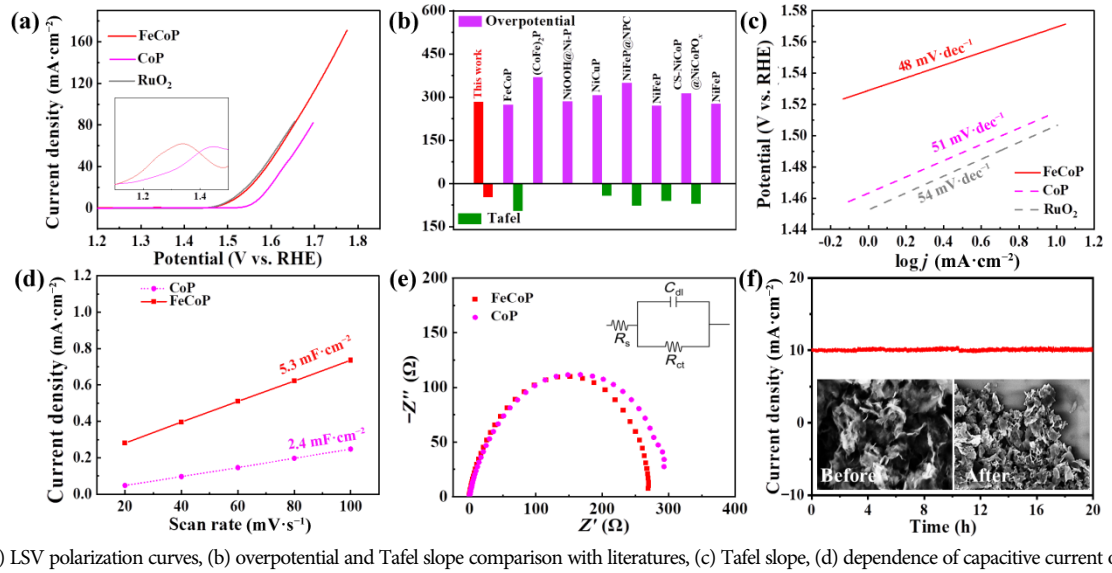

Figure 4 (a) LSV polarization curves, (b) overpotential and Tafel slope comparison with literatures, (c) Tafel slope, (d) dependence of capacitive current on scan rates, (e) Nyquist plots, and (f) stability tested using chronoamperometry for OER.

utilized to investigate changes of bonding states of absorbed H_2O on the FeCoP surface (Fig. 5(a)) [37]. When the electrocatalyst was soaked in the electrolyte, the bending vibration peak of O-H bond was found at 1604 cm^{-1} [38]. As water splitting proceeded, this peak showed a red-shift, demonstrating that O-H bonds became weaker as the water splitting continued. The effective breaking down of O-H bonds has provided sufficient H^* species for the following Heyrovsky and Tafel steps, assuring excellent water splitting performance of the FeCoP.

Meanwhile, theoretical calculations were conducted to explore the mechanisms underlying the adsorption of H_2O molecules on the surface of FeCoP (Figs. 5(b) and 5(c). The obtained results indicate that the adsorption energy of subcrystalline FeCoP for H_2O (−1.29 eV) is smaller than that of crystalline FeCoP (−1.14), suggesting that defects associated with unsaturated atoms in the subcrystalline FeCoP are more liable to adsorb H_2O molecules and speed up the kinetics of Volmer step. Based on the above experiential results, the mechanism of water splitting in alkaline medium can be elucidated by considering that the amorphous regions act as sites for the adsorption and dissociation of water molecules. Subsequently, the electocatalytic desorption of H_2 and O_2 readily takes place at the short-range ordered structures of FeCoP.

Figure 6 shows the obtained XPS spectra of FeCoP before and after the HER and OER processes, which were examined to understand the elemental composition and valence state changes

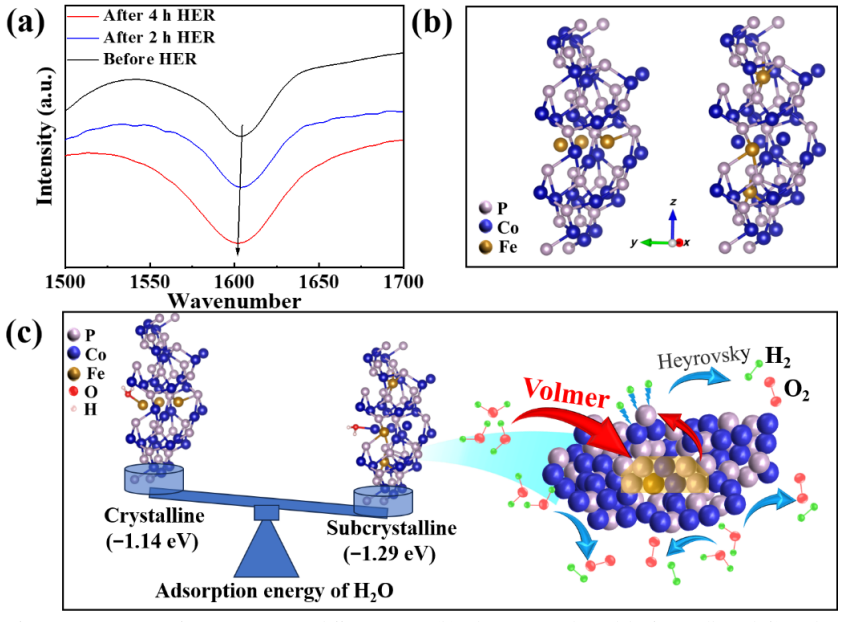

Figure 5 (a) FTIR spectrum of H-OH in FeCoP after experiencing different time. (b) The structural model of crystalline (left) and subcrystalline (right) FeCoP. (c) The analysis of water splitting mechanism.

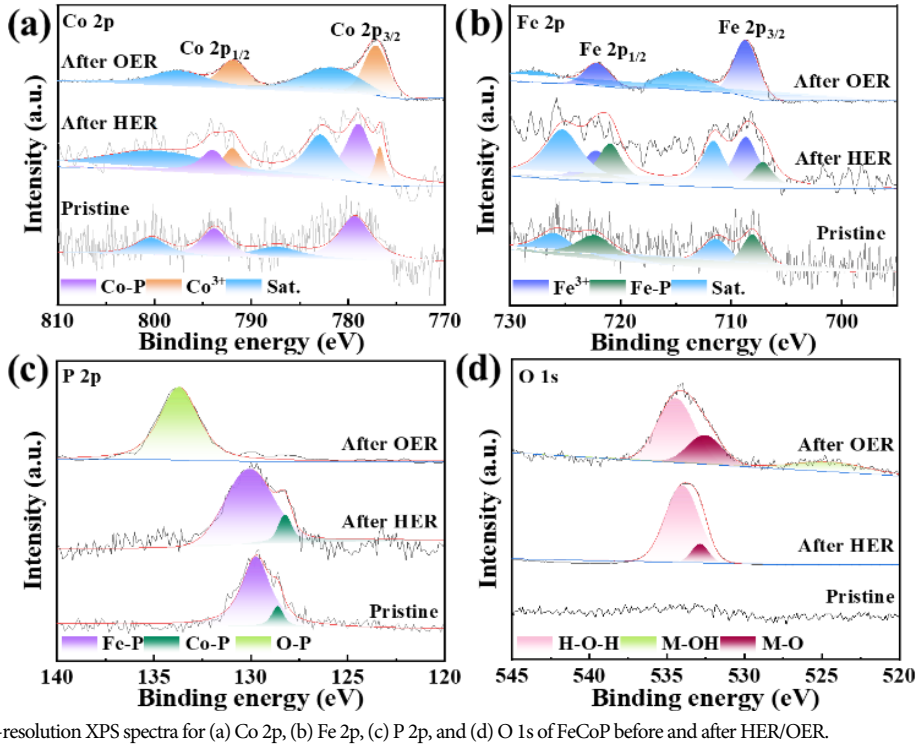

Figure 6 Contrast high-resolution XPS spectra for (a) Co 2p, (b) Fe 2p, (c) P 2p, and (d) O 1s of FeCoP before and after HER/OER.

on the surface. For high-resolution Co 2p spectra in Fig. 6(a), the Co^{3+} peaks were observed at the binding energies of 791.7 eV ($2p_{1/2}$) and 776.6 eV ($2p_{3/2}$) after the HER, indicating a portion of $Co^{\delta+}$ ($0 < \delta < 2$) in Co-P were oxidized during the HER process. For the spectrum of Fe 2p (Fig. 6(b)), the peaks corresponding to $Fe^{\delta+}$ ($0 < \delta < 2$) in Fe-P are shifted to 720.8 eV ($2p_{1/2}$) and 707 eV ($2p_{3/2}$) from 722.2 eV ($2p_{1/2}$) and 708 eV ($2p_{3/2}$), respectively, indicating a decrease in Fe electron cloud density. In addition, Fe^{3+} peaks at 722.2 eV ($2p_{1/2}$) and 708 eV ($2p_{3/2}$) appear after the HER, indicating the oxidation of some Fe in the Fe-P. The higher proportion of Co^{3+} and Fe^{3+} peaks indicates that the FeCoP has a strong electron donating capability due to the phosphating effect [39]. It is worth noting that after the OER, only the characteristic peaks and corresponding satellite peaks of oxidized Co^{3+} and Fe^{3+} exist in the spectra of Co 2p and Fe 2p as shown in Figs. 6(a) and 6(b). The disappearance of the original Co-P and Fe-P characteristic peaks confirms that the FeCoP has been oxidized during the OER.

The high-resolution XPS spectrum of P 2p (Fig. 6(c)) only exists the O-P characteristic peak located at 133.7 eV after OER and the characteristic peak of M-O appeared at 524.4 eV in the O 1s spectrum (Fig. 6(d)), further proving that phosphides were oxidized during the OER process. The high-valence state species of Co^{3+} and Fe^{3+} have more 3d electron orbits and thus higher electron-accepting ability than those of low-valence metal ($Co^{\delta+}$ and $Fe^{\delta+}$, $0 < \delta < 2$), facilitating the electrocatalytic OER process and resulting in the higher electrochemical activity [40, 41]. On the other hand, the peak of M-OH was found at the binding energy of 525.0 eV, which is believed to be originated from the OH^- generated from the Volmer step attacking the adjacent $Co^{\delta+}$ and $Fe^{\delta+}$ centers at the surface of the catalysts. These results indicate that the active substances of HER and OER come from the hydroxides and oxidized species on the surface of catalyst [42], which has significantly increased the active sites for both the HER and OER, and thus reduce their reaction energy barriers, finally improving the overall water splitting activities [43]. In general, the sluggish kinetics of the overall water splitting is caused by the increased difficulty for the cleavage of HO-H bonds in water molecules than those in the hydrated protons [44]. The capture of H^+ by $P^{\delta-}$ and the adsorption of OH^- by the unfilled d-orbitals of $Fe^{\delta+}/Co^{\delta+}$ promote the FeCoP to effectively catalyze the break-up of HO-H bonds [45]. Besides, the FeCoP maintains the subcrystalline feature. Both these effects lead to better corrosion-resistance and catalytic activity.

Based on the above discussions, the excellent alkaline HER and OER performances of FeCoP can be summarized as following. (i) The ultrathin FeCoP nanosheets augment the number of active sites, extending from the surface into the bulk of the material, thereby enhancing the catalytic efficiency of each individual site. (ii) Defects associated with the unsaturated atoms in the subcrystalline structure can act as the active sites to enhance electrocatalytic activities. (iii) The d-electronic configuration of Co after doping with Fe can be modified to reduce the reaction energy barrier. (iv) The short-range ordering nature of subcrystalline materials can effectively resist the corrosion of electrolytes on electrocatalysts during their applications, thus improving their stability.

The excellent electrocatalytic performance for both HER and OER suggests that FeCoP has the potential applications for commercial overall water splitting. The synthesized FeCoP was applied as the working electrodes (as both anode and cathode) for overall water splitting (Fig. 7). The electric energy comes from the solar photovoltaic system. When the overpotentials are 1.50 and 1.80 V vs. RHE, the corresponding current densities are 10 and 200 $mA{\cdot}cm^{-2}$ (Fig. 7(a)). Moreover, the LSV curves only show minor decay of 8% after chronopotentiometry test. Such a current density can be maintained after the chronoamperometry measurements for 12 h, revealing its excellent durability (Fig. 7(b)). The combined system for generating green hydrogen from overall water splitting and its application is composed of photovoltaic system, accumulator, water electrolysis system (FeCoP as bifunctional catalysts), and hydrogen fuel cell with fan (Figs. 7(c) and 7(d)). Specifically, the renewable electrical energy generated by the photovoltaic system is stored in an accumulator, which is then utilized for water electrolysis, thereby producing green hydrogen. The green hydrogen thus obtained supplies a fuel cell to drive a fan, which can continuously run for 10 h. Thereby the potential for renewable energy solutions is demonstrated in applications of green hydrogen.

4 Conclusions

In summary, subcrystalline FeCoP ultrathin nanosheets of were constructed as an efficient alkaline water splitting catalyst. The

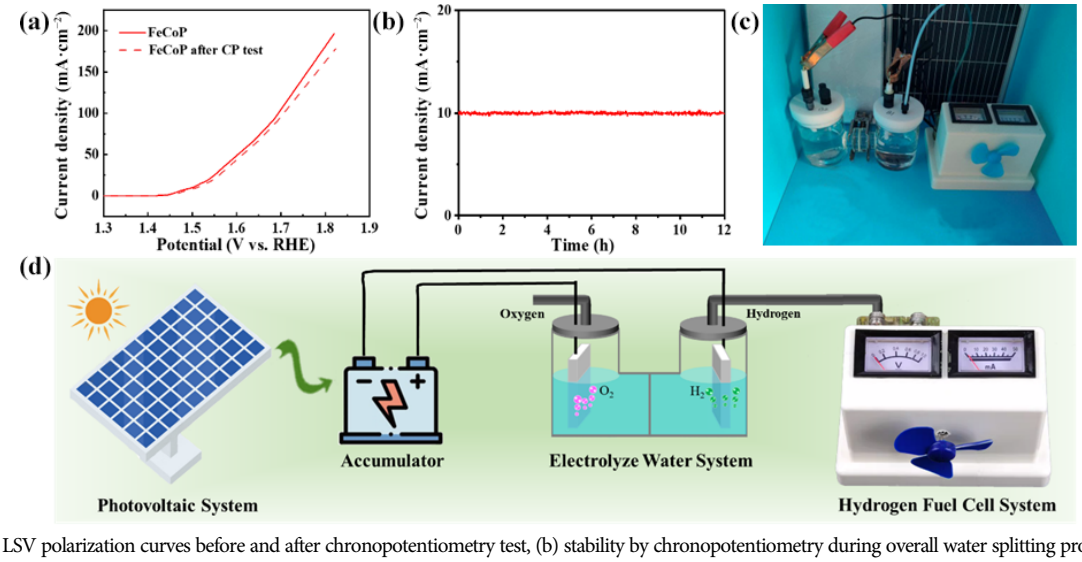

Figure 7 (a) LSV polarization curves before and after chronopotentiometry test, (b) stability by chronopotentiometry during overall water splitting process, (c) overall water splitting by renewable electrical energy come from photovoltaic system, and (d) application of green hydrogen.

good performance of activity is benefited from that the ultrathin nanosheets and the subcrystalline structures can expose more active sites, the optimization of the metal d-electronic configuration achieves good adsorption, and short-range order can ensure high structural stability. The good performance of FeCoP as the bifunctional catalysts for the overall water splitting can be proved and using electricity from solar photovoltaic systems. This research offers not only a new approach to use 2D catalyst for alkaline overall water splitting by accelerating kinetics, but also new pathways of designing subcrystalline electrocatalysts.

Acknowledgements

This work is financially supported by the National Natural Science Foundation (NSFC) (No: 22171212), Science and Technology Committee of Shanghai Municipality (Nos: 21160710300, 2022-4-YB-12) by China, and International Exchange Grant (IEC/NSFC/201078) through Royal Society UK and NSFC.

Electronic Supplementary Material: Supplementary material (further details of the SEM images, CV curves, LSV curves, *I-V* curve, Faradaic efficiency values and comparative tables of performance) is available in the online version of this article at https://doi.org/10.26599/NRE.2024.9120129.

Declaration of conflicting interests

The authors declare no conflicting interests regarding the content of this article.

Data availability

All data needed to support the conclusions in the paper are presented in the manuscript and/or the Supplementary Materials. Additional data related to this paper may be requested from the corresponding author upon request.

References

[1] Jing, X. Y.; Mu, Y.; Gao, Z. M.; Dong, X. Y.; Meng, C. G.; Huang, C.; Zhang, Y. F. Intermetallic ferric nickel silicide alloy derived from magadiite by magnesiothermic reaction as bifunctional electrocatalyst for overall water splitting. *Nano Res. Energy* **2024**, *3*, e9120104.

[2] Li, L.; Hu, J. S.; Wei, Z. D. Preface to special issue on water electrolysis for hydrogen production. *J. Electrochem.* **2022**, *28*, 22214000.

[3] Mu, X. Q.; Gu, X. Y.; Dai, S. P.; Chen, J. B.; Cui, Y. J.; Chen, Q.; Yu, M.; Chen, C. Y.; Liu, S. L.; Mu, S. C. Breaking the symmetry of single-atom catalysts enables an extremely low energy barrier and high stability for large-current-density water splitting. *Energy Environ. Sci.* **2022**, *15*, 4048–4057.

[4] Xu, S. R.; Feng, S. H.; Yu, Y.; Xue, D. P.; Liu, M. L.; Wang, C.; Zhao, K. Y.; Xu, B. J.; Zhang, J. N. Dual-site segmentally synergistic catalysis mechanism: Boosting $CoFeS_x$ nanocluster for sustainable water oxidation. *Nat. Commun.* **2024**, *15*, 1720.

[5] Huang, C. J.; Xu, H. M.; Shuai, T. Y.; Zhan, Q. N.; Zhang, Z. J.; Li, G. R. A review of modulation strategies for improving catalytic performance of transition metal phosphides for oxygen evolution reaction. *Appl. Catal. B: Environ.* **2023**, *325*, 122313.

[6] Zhou, X. Y.; Yang, T. T.; Li, T.; Zi, Y. J.; Zhang, S. J.; Yang, L.; Liu, Y. K.; Yang, J.; Tang, J. J. *In-situ* fabrication of carbon compound NiFeMo-P anchored on nickel foam as bi-functional catalyst for boosting overall water splitting. *Nano Res. Energy* **2023**, *2*, e9120086.

[7] Li, Y.; Dong, Z. H.; Jiao, L. F. Multifunctional transition metal-based phosphides in energy-related electrocatalysis. *Adv. Energy Mater.* **2020**, *10*, 1902104.

[8] Agarwal, A.; Sankapal, B. R. Metal phosphides: Topical advances in the design of supercapacitors. *J. Mater. Chem. A* **2021**, *9*, 20241–20276.

[9] Naderi, L.; Shahrokhian, S. Nickel vanadium sulfide grown on nickel copper phosphide dendrites/Cu fibers for fabrication of all-solid-state wire-type micro-supercapacitors. *Chem. Eng. J.* **2020**, *392*, 124880.

[10] Indra, A.; Menezes, P. W.; Zaharieva, I.; Baktash, E.; Pfrommer, J.; Schwarze, M.; Dau, H.; Driess, M. Active mixed-valent MnO_x water oxidation catalysts through partial oxidation (corrosion) of nanostructured MnO particles. *Angew. Chem., Int. Ed.* **2013**, *52*, 13206–13210.

[11] Zhang, W. Q.; Li, Y.; Zhou, L. X.; Zheng, Q. J.; Xie, F. Y.; Lam, K. H.; Lin, D. M. Ultrathin amorphous CoFeP nanosheets derived from CoFe LDHs by partial phosphating as excellent bifunctional catalysts for overall water splitting. *Electrochim. Acta* **2019**, *323*, 134595.

[12] Wang, X. G.; Li, W.; Xiong, D. H.; Petrovykh, D. Y.; Liu, L. F. Bifunctional nickel phosphide nanocatalysts supported on carbon fiber paper for highly efficient and stable overall water splitting. *Adv. Funct. Mater.* **2016**, *26*, 4067–4077.

[13] Zhao, L.; Wen, M.; Tian, Y. K.; Wu, Q. S.; Fu, Y. Q. A novel structure of quasi-monolayered NiCo-bimetal-phosphide for superior electrochemical performance. *J. Energy Chem.* **2022**, *74*, 203–211.

[14] Liu, J. Z.; Nai, J. W.; You, T. T.; An, P. F.; Zhang, J.; Ma, G. S.; Niu, X. G.; Liang, C. Y.; Yang, S. H.; Guo, L. The flexibility of an amorphous cobalt hydroxide nanomaterial promotes the electrocatalysis of oxygen evolution reaction. *Small* **2018**, *14*, 1703514.

[15] Chen, D. W.; Dong, C. L.; Zou, Y. Q.; Su, D.; Huang, Y. C.; Tao, L.; Dou, S.; Shen, S. H.; Wang, S. Y. *In situ* evolution of highly dispersed amorphous CoO_x clusters for oxygen evolution reaction. *Nanoscale* **2017**, *9*, 11969–11975.

[16] Zhou, Y.; Fan, H. J. Progress and challenge of amorphous catalysts for electrochemical water splitting. *ACS Mater. Lett.* **2021**, *3*, 136–147.

[17] Liu, J. Z.; Ji, Y. F.; Nai, J. W.; Niu, X. G.; Luo, Y.; Guo, L.; Yang, S. H. Ultrathin amorphous cobalt-vanadium hydr(oxy)oxide catalysts for the oxygen evolution reaction. *Energy Environ. Sci.* **2018**, *11*, 1736–1741.

[18] Risch, M.; Ringleb, F.; Kohlhoff, M.; Bogdanoff, P.; Chernev, P.; Zaharieva, I.; Dau, H. Water oxidation by amorphous cobalt-based oxides: *In situ* tracking of redox transitions and mode of catalysis. *Energy Environ. Sci.* **2015**, *8*, 661–674.

[19] Deng, K.; Mao, Q. Q.; Wang, W. X.; Wang, P.; Wang, Z. Q.; Xu, Y.; Li, X. N.; Wang, H. J.; Wang, L. Defect-rich low-crystalline Rh metallene for efficient chlorine-free H_2 production by hydrazine-assisted seawater splitting. *Appl. Catal. B: Environ.* **2022**, *310*, 121338.

[20] Cai, W. Z.; Chen, R.; Yang, H. B.; Tao, H. B.; Wang, H. Y.; Tao, H. B.; Wang, H. Y.; Gao, J. J.; Liu, W.; Liu, S.; Hung, S. F.; Liu, B. Amorphous versus crystalline in water oxidation catalysis: A case study of NiFe alloy. *Nano Lett.* **2020**, *20*, 4278–4285.

[21] Tan, Y. W.; Wang, H.; Liu, P.; Shen, Y. H.; Cheng, C.; Hirata, A.; Fujita, T.; Tang, Z.; Chen, M. W. Versatile nanoporous bimetallic phosphides towards electrochemical water splitting. *Energy Environ. Sci.* **2016**, *9*, 2257–2261.

[22] Jiang, N.; You, B.; Sheng, M. L.; Sun, Y. J. Electrodeposited cobalt-phosphorous-derived films as competent bifunctional catalysts for overall water splitting. *Angew. Chem., Int. Ed.* **2015**, *54*, 6251–6054.

[23] Liu, Y. R.; Du, Y. M.; Gao, W. K.; Dong, B.; Han, Y.; Wang, L. Surface phosphorsulfurization of $NiCo_2O_4$ nanoneedles supported on carbon cloth with enhanced electrocatalytic activity for hydrogen evolution. *Electrochim. Acta* **2018**, *290*, 339–346.

[24] Du, Y. M.; Zhang, M. J.; Wang, Z. C.; Liu, Y. R.; Liu, Y. J.; Geng, Y. L.; Wang, L. A self-templating method for metal-organic

frameworks to construct multi-shelled bimetallic phosphide hollow microspheres as highly efficient electrocatalysts for hydrogen evolution reaction. *J. Mater. Chem. A* **2019**, *7*, 8602–8608.
[25] Qu, G. X.; Zhao, Y. W.; Zhao, G. L.; Zhou, Y.; Cai, S. K.; Kang, Y. J.; Xu, C. Ultrahigh length-to-diameter ratio nickel phosphide nanowires as pH-wide electrocatalyst for efficient hydrogen evolution. *Electrochim. Acta* **2019**, *298*, 943–949.
[26] Li, M.; Liu, T. T.; Bo, X. J.; Zhou, M.; Guo, L. P.; Guo, S. J. Hybrid carbon nanowire networks with Fe-P bond active site for efficient oxygen/hydrogen-based electrocatalysis. *Nano Energy* **2017**, *33*, 221–228.
[27] Montgomery, C. L.; Amtawong, J.; Jordan, A. M.; Kurtz, D. A.; Dempsey, J. L. Proton transfer kinetics of transition metal hydride complexes and implications for fuel-forming reactions. *Chem. Soc. Rev.* **2023**, *52*, 7137–7169.
[28] Jiang, P.; Liu, Q.; Liang, Y. H.; Tian, J. Q.; Asiri, A. M.; Sun, X. P. A cost-effective 3D hydrogen evolution cathode with high catalytic activity: FeP nanowire array as the active phase. *Angew. Chem., Int. Ed.* **2014**, *53*, 12855–12859.
[29] Sun, H.; Min, Y. X.; Yang, W. J.; Lian, Y. B.; Lin, L.; Feng, K.; Deng, Z.; Chen, M. Z.; Zhong, J.; Xu, L. et al. Morphological and electronic tuning of Ni_2P through iron doping toward highly efficient water splitting. *ACS Catal.* **2019**, *9*, 8882–8892.
[30] Mahmood, N.; Yao, Y. D.; Zhang, J. W.; Pan, L.; Zhang, X. W.; Zou, J. J. Electrocatalysts for hydrogen evolution in alkaline electrolytes: Mechanisms, challenges, and prospective solutions. *Adv. Sci.* **2018**, *5*, 1700464.
[31] Su, J. Z.; Zhou, J. L.; Wang, L.; Liu, C.; Chen, Y. B. Synthesis and application of transition metal phosphides as electrocatalyst for water splitting. *Sci. Bull.* **2017**, *62*, 633–644.
[32] Jin, J.; Wang, X. Y.; Hu, Y.; Zhang, Z.; Liu, H. B.; Yin, J.; Xi, P. X. Precisely control relationship between sulfur vacancy and H absorption for boosting hydrogen evolution reaction. *Nano-Micro Lett.* **2024**, *16*, 63.
[33] Jin, J.; Yin, J.; Liu, H. B.; Huang, B. L.; Hu, Y.; Zhang, H.; Sun, M. Z.; Peng, Y.; Xi, P. X.; Yan, C. H. Atomic sulfur filling oxygen vacancies optimizes H absorption and boosts the hydrogen evolution reaction in alkaline media. *Angew. Chem., Int. Ed.* **2021**, *60*, 14117–14123.
[34] Shuai, C.; Mo, Z. L.; Niu, X. H.; Zhao, P.; Dong, Q. B.; Chen, Y.; Liu, N. J.; Guo, R. B. Nickel/cobalt bimetallic phosphides derived metal-organic frameworks as bifunctional electrocatalyst for oxygen and hydrogen evolution reaction. *J. Alloys Compd.* **2020**, *847*, 156514.
[35] Conway, B. E.; Salomon, M. Electrochemical reaction orders: Applications to the hydrogen-and oxygen-evolution reactions. *Electrochim. Acta* **1964**, *9*, 1599–1615.
[36] Nai, J. W.; Lu, Y.; Yu, L.; Wang, X.; Lou, X. W. Formation of Ni–Fe mixed diselenide nanocages as a superior oxygen evolution electrocatalyst. *Adv. Mater.* **2017**, *29*, 1703870.
[37] Danilovic, N.; Subbaraman, R.; Strmcnik, D.; Chang, K. C.; Paulikas, A. P.; Stamenkovic, V. R.; Markovic, N. M. Enhancing the alkaline hydrogen evolution reaction activity through the bifunctionality of $Ni(OH)_2$/metal catalysts. *Angew. Chem., Int. Ed.* **2012**, *51*, 12495–12498.
[38] Dong, Z. H.; Lin, F.; Yao, Y. H.; Jiao, L. F. Crystalline $Ni(OH)_2$/amorphous $NiMoO_x$ mixed-catalyst with Pt-like performance for hydrogen production. *Adv. Energy Mater.* **2019**, *9*, 1902703.
[39] Hao, J. H.; Yang, W. S.; Zhang, Z.; Tang, J. L. Metal-organic frameworks derived $Co_xFe_{1-x}P$ nanocubes for electrochemical hydrogen evolution. *Nanoscale* **2015**, *7*, 11055–11062.
[40] Jin, J.; Yin, J.; Hu, Y.; Zheng, Y.; Liu, H. B.; Wang, X. Y.; Xi, P. X.; Yan, C. H. Stabilizing sulfur sites in tetraoxygen tetrahedral coordination structure for efficient electrochemical water oxidation. *Angew. Chem., Int. Ed.* **2024**, *63*, e202313185.
[41] Lu, X. Q.; Xu, H.; Yang, T. F.; Chen, X. D.; Cheng, Z.; Hou, Q.; Lin, X. J.; Liu, S. Y.; Wei, S. X.; Wang, Z. J. Co^{3+}-rich CoFe-PBA encapsulated in ultrathin MoS_2 sheath as integrated core-shell architectures for highly efficient OER. *J. Alloy. Compd.* **2023**, *942*, 169004.
[42] Boppella, R.; Tan, J.; Yang, W.; Moon, J. Homologous CoP/NiCoP heterostructure on N-doped carbon for highly efficient and pH-universal hydrogen evolution electrocatalysis. *Adv. Funct. Mater.* **2019**, *29*, 1807976.
[43] Chai, L.; Liu, S. L.; Pei, S. T.; Wang, C. Electrodeposited amorphous cobalt-nickel-phosphide-derived films as catalysts for electrochemical overall water splitting. *Chem. Eng. J.* **2021**, *420*, 129686.
[44] Huang, Z. P.; Chen, Z. Z.; Chen, Z. B.; Lv, C. C.; Humphrey, M. G.; Zhang, C. Cobalt phosphide nanorods as an efficient electrocatalyst for the hydrogen evolution reaction. *Nano Energy* **2014**, *9*, 373–382.
[45] Wu, M. Y.; Da, P. F.; Zhang, T.; Mao, J.; Liu, H.; Ling, T. Designing hybrid NiP_2/NiO nanorod arrays for efficient alkaline hydrogen evolution. *ACS Appl. Mater. Interfaces* **2018**, *10*, 17896–17902.

Long Zhao obtained his PhD degrees from Tongji University under the supervision of Prof. Ming Wen in 2024. He received his B.E. and M.E. degrees (2016 and 2019) from Inner Mongolia University of Technology, China. His current research interests focus on the application of nanomaterials in the fields of photocatalysis and electrocatalysis.

Ming Wen is a full professor in the School of Chemical Science and Engineering at Tongji University. She received her PhD degree from chemistry department of Kinki University (Japan) in 2002. Her primary research interests cover nanomaterial & inorganic chemistry and material science with applications for energy and environments, including alloy and their oxide composite nanomaterials with controllable structures, which are achieved by various chemical interactions and controlled self-assembly.